NASA TECHNICAL NOTE

NASA TN D-6266

NASA TN D-6266

c. 1

THE LUNAR ORBITER METEOROID EXPERIMENTS

Description and Results From Five Spacecraft

by Gary W. Grew and Charles A. Gurtler

Langley Research Center
Hampton, Va. 23365

NATIONAL AERONAUTICS AND SPACE ADMINISTRATION • WASHINGTON, D. C. • JUNE 1971

1. Report No.	2. Government Accession No.	3. Recipient's Catalog No.
NASA TN D-6266		

4. Title and Subtitle	5. Report Date
THE LUNAR ORBITER METEOROID EXPERIMENTS – DESCRIPTION AND RESULTS FROM FIVE SPACECRAFT	June 1971
	6. Performing Organization Code
7. Author(s)	8. Performing Organization Report No.
Gary W. Grew and Charles A. Gurtler	L-7600
	10. Work Unit No.
9. Performing Organization Name and Address	815-00-00-00
NASA Langley Research Center Hampton, Va. 23365	11. Contract or Grant No.
	13. Type of Report and Period Covered
12. Sponsoring Agency Name and Address	Technical Note
National Aeronautics and Space Administration Washington, D.C. 20546	14. Sponsoring Agency Code

15. Supplementary Notes

16. Abstract

Meteoroid experiments by five Lunar Orbiters have provided a direct measurement in the near-lunar environment of the rate of meteoroid penetration of 0.025-mm-thick beryllium-copper. Each experiment used 20 pressurized-cell detectors having a total effective exposed area of 0.186 m^2. The spacecraft carrying the cells were in both equatorial and polar orbits; altitudes ranged between 30 and 6200 km. Data collected continuously for 17 months indicate that the rate of penetration in the lunar environment is approximately half the rate in the near-earth environment as measured by detectors of the same type aboard Explorers XVI and XXIII.

17. Key Words (Suggested by Author(s))	18. Distribution Statement
Meteroids Lunar Orbiter	Unclassified – Unlimited

19. Security Classif. (of this report)	20. Security Classif. (of this page)	21. No. of Pages	22. Price*
Unclassified	Unclassified	43	$3.00

*For sale by the National Technical Information Service, Springfield, Virginia 22151

THE LUNAR ORBITER METEOROID EXPERIMENTS

DESCRIPTION AND RESULTS FROM FIVE SPACECRAFT

By Gary W. Grew and Charles A. Gurtler
Langley Research Center

SUMMARY

Meteoroid experiments by five Lunar Orbiters have provided a direct measurement in the near-lunar environment of the rate of meteoroid penetration of 0.025-mm-thick beryllium-copper. Each experiment used 20 pressurized-cell detectors having a total effective exposed area of 0.186 m^2. The spacecraft carrying the cells were in both equatorial and polar orbits; altitudes ranged between 30 and 6200 km. Data collected continuously for 17 months indicate that the rate of penetration in the lunar environment is approximately half the rate in the near-earth environment as measured by detectors of the same type aboard Explorers XVI and XXIII.

INTRODUCTION

The primary mission of the Lunar Orbiter spacecraft was to obtain closeup photographs of the potential landing sites for the Apollo missions. This objective was accomplished, and, in addition, 99 percent of the lunar surface was photographed with a resolution at least 10 times better than earth-based telescopes could provide. Secondary mission objectives were to obtain meteoroid, radiation, and selenodetic data. The meteoroid experiment is the only mission objective discussed in this paper.

Penetrations by meteoroids were measured by five Lunar Orbiters for assessment of the hazard to the pressurized camera system and for comparison of the penetration rate (for a metal skin) in the vicinity of the moon with rates measured near the earth. Such measurements would also help to determine the protection required for spacesuits, instruments, and spacecraft for the Apollo missions.

Estimates of the hazard near the moon have ranged from somewhat less to several orders of magnitude greater than the hazard near the earth. A major uncertainty is the contribution by secondary meteoroids created by impacts of primary meteoroids on the moon.

Before the Lunar Orbiters, the only measurements by satellites of meteoroid flux near the moon were made by Luna 10 with piezoelectric detectors that were sensitive to particle impacts; impacts were recorded between 355 and 1050 km, the average rate of 4×10^{-3} m^{-2}-sec^{-1} exceeding the average for interplanetary space by about two orders of magnitude (ref. 1).

SYMBOLS

A	area
A_e	effective area
A_p	projected area
$\overline{A}_p$	average projected area
a	point on X-axis
b_1, b_2, b_3, b_4	constants which define equation of a plane
c	point on Z-axis
d	point on Y-axis
$\overline{dA}_\alpha$	average element of area for a given angle α
dw	element of solid angle
$f(\gamma)d\gamma$	function equal to $\cos(\theta - \alpha)\sin^2\phi \, d\alpha \, d\theta \, d\phi$
G	gravitational increase in flux factor
k_1, k_2	constants of coordinate transformation equations
M(n)	sum of squares of deviations of n_i
N	total number of penetrations
n	number of penetrations

n_i	number of penetrations for ith spacecraft
P_n	probability of occurrence of n penetrations
p	probability of occurrence of a single penetration
R	correlation coefficient
R_p	distance of planet from sun in astronomical units
r	radius
r_p	radius of planet
r_s	distance from planet's center
s_1, s_2	constants which define edge of solar panel in terms of ϕ in a given plane
T	time-area exposure, m^2-days
T_i	time-area exposure for ith spacecraft, m^2-days
V_e	escape velocity from earth's surface
V_p	escape velocity from planet's surface
X,Y,Z	axes
X',Y',Z' X'',Y'',Z''	transformed axes
x,y,z	coordinate along X-, Y-, and Z-axis, respectively
x',y',z' x'',y'',z''	coordinates along transformed axes
$\alpha, \alpha_1, \alpha_2$	angles between $\overrightarrow{dA}$ and X-axis in X-Y plane
β, Δ	angles used in defining angle κ

$\epsilon = \kappa + \pi$

$\theta, \theta_1, \theta_2$ angles measured in X-Y plane

κ largest angle in X-Y plane for a given α in which dA is not shielded from space by a lower detector

σ angle of rotation

ϕ, ϕ_1, ϕ_2 angles measured from the Z-axis

ψ meteoroid penetration rate, penetrations-m^{-2}-day^{-1}

ψ_M maximum likelihood estimator of meteoroid penetration rate, penetrations-m^{-2}-day^{-1}

ψ'_M ψ_M derived by minimizing deviations of T_i

$\omega, \omega_1, \omega_2, \omega_3, \omega_4$ angles measured between $\overrightarrow{dA}$ and some point on edge of a solar panel in X-Y plane

ORBITAL AND ATTITUDE PARAMETERS

The first Lunar Orbiter spacecraft was launched on August 10, 1966, and the succeeding spacecraft were launched at 3-month intervals, as shown in table I. All spacecraft have impacted the lunar surface upon command except Lunar Orbiter IV. All communication with this spacecraft was lost on July 17, 1967. Calculations from final tracking data indicate that it decayed through orbital perturbations and impacted the moon during the month of October 1967.

The orbital parameters for the five spacecraft are shown in table II. The parameters listed are for the first orbit after a spacecraft was maneuvered into a new orbit. As a result of perturbations, the perilune and apolune extremes attained by any spacecraft were about 30 and 6200 km, respectively.

During the photographic phase of the mission, precise knowledge of attitude was necessary in order to properly maneuver and orient the spacecraft for each lunar site photographed. The spacecraft, therefore, required an attitude control subsystem which consisted basically of a control engine, sun sensors, Canopus star tracker, inertial reference unit, and thrusters, as shown in figure 1. The spacecraft could be maneuvered

about any of the three axes, as designated in the figure. The inertial reference during the 30-day photographic mission for each spacecraft was defined by a line to the sun (+X-axis) and a line to Canopus (approximately along the +Y-axis). Because of inherent drifting of the gyros, the inertial reference required periodic updating.

The original plan was to maintain the sun reference and allow the spacecraft to drift about the roll axis during the extended mission, which was the remaining life of the spacecraft after completion of the photographic mission. However, because of thermal problems, the spacecraft were required to maintain an off-sun attitude. Because of gyro drift, the spacecraft were programed to periodically acquire sun for reference and then to pitch off sun at a given angle, which varied with spacecraft, between 25° and 60°. Although the spacecraft were allowed to drift about the roll axis throughout most of the extended missions, updating was required occasionally when the spacecraft were positioned for orbital changes and for special experiments. These reference points are useful in determining attitude positions of the spacecraft for times between up-dates by applying the known gyro drift rates. Spacecraft attitude during times of penetration (discussed in a subsequent paragraph) was determined by this method.

METEOROID EXPERIMENT

The Lunar Orbiters carried pressurized-cell meteoroid detectors like the ones flown near earth aboard Explorers XVI and XXIII. Each detector is a pressurized semicylinder with a pressure-sensitive switch; the cylindrical surface of the detector is the test material. (See fig. 2.) On the basis of experience from the Explorer experiments, the test material selected for the Lunar Orbiters was 0.025-mm-thick beryllium-copper. Gas pressure holds the switch closed, but when the pressure is released by penetration of the test material, the switch returns to open and stays in this position as a permanent record of the penetration. Whenever the condition of the detector is telemetered, new penetrations are indicated and previously indicated penetrations are verified.

Weight allocation permitted the experiment on each of the five spacecraft to consist of 20 pressurized-cell detectors arranged in a ring outside the thermal blanket (fig. 3). A thermal blanket was placed around the spacecraft to provide for a temperature-controlled environment for the camera package and other instrumentation. Since 20 detectors could not be placed in a single ring, two were placed side by side in each of five positions on the ring. Each detector, being a semicylinder, shows half as much area when viewed from the side as when viewed from the top. When the ring is viewed from the small end of the spacecraft, along the major axis, the full ring of detectors is visible in side view. When the spacecraft is viewed from a direction normal to the major axis, the tops of approximately half the detectors are visible. Thus, about the same area is presented in both directions.

The total area of the test material aboard each spacecraft was 0.282 m^2. Partial shielding by the solar-cell panels, antennas, and other components reduced this area by 34 percent; therefore, the effective area was 0.186 m^2. Of course, the shielding also compromised the isotropy of exposure of the test material to the environment. The method of calculating the effective area of each detector, which is found in the appendix, is summarized briefly here. First, detectors with approximately the same geometry with respect to the spacecraft were identified. As a result, the 20 detectors could be divided into 6 cases – the detectors within each case having the same geometry. Then the average projected area for each case was calculated by taking into account the shielding factors. By means of the formula derived in the appendix, the effective area for each case could be calculated directly from the average projected area for each case. From these results the total effective area of the 20 detectors was calculated to be 0.186 m^2. The average effective area of any detector is, therefore, 0.186/20 or 0.0093 m^2, which is used in the computation of the penetration rates.

The spacecraft was nominally oriented with the large end, which carries the solar-cell panels, pointing toward the sun. The tapered midsection created a 20^o half-angle conical blindspot for the detectors in the direction of the sun, and the solar panels blocked about half the conical annulus between 20^o and 60^o. Since data were collected for more than 1 year, the combined missions covered at least one complete orbit of the earth-moon system about the sun.

When the telemeter was activated, the condition of the detectors was transmitted every 23 seconds. However, there were gaps in the data as a result of earth shadow (blackout) and competition with other spacecraft in using the Deep Space Network.

PENETRATION DATA

The penetration data for the five spacecraft are given in table III in order of occurrence. One penetration, not indicated in the table, occurred accidentally on Lunar Orbiter III prior to launch at a time too late for replacement. The dates listed are for the first interrogation in which each new penetration was recorded. The last column lists the uncertainty in the time of occurrence of each penetration. The minimum and maximum uncertainties were 23 seconds and 120 hours. The time resolutions for the penetrations are quite adequate for the calculations of the penetration rates and permitted a total uncertainty in the time-area exposure for all five spacecraft of only 0.1 percent.

By assuming that the five Lunar Orbiters sampled the same meteoroid population (discussed under "Data Analysis"), the average penetration rates were calculated by division of the total number of penetrations by the total time-area product,

$$\psi = \frac{N}{T} \tag{1}$$

where ψ is the penetration rate (penetrations per square meter per day), N is the total number of penetrations, and T is the product of time (days) and area (square meters) of exposure. In determining the exposed time-area, the gradual loss in area as detectors are penetrated must be considered; whenever a sensor is penetrated, the effective area is reduced and the reduced area is effective until the next penetration. The number of penetrations and the exposed time-area products for each spacecraft are given in table IV.

The five Lunar Orbiters recorded 22 penetrations during a time-area exposure of 139.0 m^2-days; the corresponding average rate of penetration was 0.16 m^{-2}-day^{-1}. In addition, the detectors were exposed to 3.5 m^2-days during transit between the earth and moon, with no penetrations. These data are compared (table V) with data collected with similar test material by Explorers XVI and XXIII near the earth. Explorer XVI collected 44 penetrations during a time-area exposure of 132.9 m^{-2}-day (ψ = 0.33 m^{-2}-day^{-1}), and Explorer XXIII collected 50 penetrations during an exposure of 139.9 m^2-days (ψ = 0.36 m^{-2}-day^{-1}). Both the Lunar Orbiter and Explorer XXIII periods covered at least 1 year, and the total time-area exposures were almost the same.

Figure 4, a plot of rate of penetration as a function of thickness of test material, shows (a) the Lunar Orbiter average rate of penetration of 0.16 m^{-2}-day^{-1}, with confidence limits (confidence coefficient, 0.95), (b) the rates measured near earth by Explorers XVI and XXIII (refs. 2 and 3), and (c) Whipple's 1963 "best estimate" (ref. 4) converted to penetration rate (ref. 3). The confidence limits were computed by using the chi-square distribution in the manner described in reference 2. The limits on the Lunar Orbiter data indicate that one can expect with 95-percent confidence that the penetration rate will be between 0.10 and 0.27 m^{-2}-day^{-1}.

The penetration rates presented thus far are not corrected for earth and lunar shielding. The Explorer detectors were shielded from 1/4 of space by the earth; the Lunar Orbiter detectors were shielded, on the average, from 1/7 of space by the moon. To convert these rates to the no-shielding condition for comparison purposes, the Explorer penetration rates are multiplied by a factor of 4/3 and the Lunar Orbiter rate is multiplied by a factor of 7/6. The resultant rates for the no-shielding condition would be equal to 0.44 and 0.48 m^{-2}-day^{-1} for Explorers XVI and XXIII, respectively, as compared with 0.19 m^{-2}-day^{-1} for the Lunar Orbiters.

The meteoroid penetration rate measured by Lunar Orbiters was several orders of magnitude less than that measured with piezoelectric sensors aboard Luna 10 interpreted in terms of rate of penetration. However, piezoelectric sensors have consistently

indicated greater rates of meteoroid flux than have penetration detectors near earth; one explanation could be the sensitivity of piezoelectric devices to noise of acoustic, thermal, or electrical origin (refs. 5 and 6).

DATA ANALYSIS

The penetration data from the five Lunar Orbiter spacecraft were examined in detail in an attempt to determine if the data were consistent from spacecraft to spacecraft, that is, if each spacecraft sampled approximately the same meteoroid population. This examination was necessary because of the small statistical samples of penetrations, the wide spread in penetrations (0 to 10), and the wide spread of time-area exposure (11.8 to 45.8 m^2-days).

A means of determining the consistency of the data is to calculate the maximum likelihood estimator (MLE) of the true mean penetration rate from the five separate experiments and to determine from this result the correlation coefficient as defined in the following paragraphs.

The maximum likelihood estimator of the penetration rate ψ_M can be found by minimizing the expression

$$M(n) = \sum_{i=1}^{i=5} \left(n_i - \psi_M T_i\right)^2 \tag{2}$$

where n_i is the number of penetrations for the ith spacecraft and T_i is the time-area exposure for the ith spacecraft (refs. 7 and 8). To determine ψ_M, $M(n)$ is differentiated with respect to ψ_M and set equal to zero, that is,

$$\frac{\partial M(n)}{\partial \psi_M} = \sum \frac{\partial}{\partial \psi_M}\left(n_i - \psi_M T_i\right)^2 = 0 \tag{3}$$

or

$$\sum 2\left(-T_i\right)\left(n_i - \psi_M T_i\right) = 0 \tag{4}$$

or

$$-\sum n_i T_i + \psi_M \sum T_i^2 = 0 \tag{5}$$

Therefore,

$$\psi_M = \frac{\sum n_i T_i}{\sum T_i^2} \tag{6}$$

(The index i has been dropped from the summation symbol for convenience.) In essence, equation (6) is the MLE of ψ found by performing a least-squares fit to the five sets of data in table IV and by assuming that the expression

$$\psi = \frac{n}{T} \tag{7}$$

is a true parametric equation describing the meteoroid population. By substituting the data from table IV into equation (6), the MLE of ψ is equal to 0.17 m^{-2}-day^{-1} which is in good agreement with the value calculated from equation (1).

A factor required to determine the correlation coefficient (refs. 8 and 9) is found by interchanging the parameters n_i and T_i in equation (6), or

$$\frac{1}{\psi'_M} = \frac{\sum n_i T_i}{\sum n_i^2} \tag{8}$$

The MLE of ψ would be ψ'_M if the deviations of T_i were minimized instead of n_i as in the case of equation (3). The correct MLE of ψ is given by equation (6) because the uncertainty of the data is in the number of penetrations. The correlation coefficient R (called r in refs. 8 and 9) can now be found from the expression

$$R = \frac{(\psi_M)^{1/2}}{(\psi'_M)^{1/2}} \tag{9}$$

Substituting equations (6) and (8) into equation (9) results in

$$R = \frac{\sum n_i T_i}{\left(\sum n_i^2 \sum T_i^2\right)^{1/2}} \tag{10}$$

If $R = 0$ there is no correlation between equation (7) and the five sets of Lunar Orbiter data. If, on the other hand, $R = 1$ there would be perfect correlation, that is, n_i/T_i for each spacecraft would be exactly equal. For the five experiments, R was calculated

to be 0.94. From tables (ref. 8) it can be determined that there is less than a 2-percent chance that the five sets of data sampling different meteoroid populations would have R = 0.94. Thus, this analysis shows that there is good justification for assuming that the five Lunar Orbiter meteoroid experiments sampled the same meteoroid population, whose penetration rate can be expressed by equation (7).

DIRECTIONALITY OF METEOROIDS

The calculated penetration rate from the Lunar Orbiter data was based on the assumption that the meteoroid flux was omnidirectional. If the flux is highly directional, the measured penetration rate would be a function of the average spacecraft orientation during the five missions. Directionality would not be a significant factor in determining the rate provided that the spacecraft had randomly tumbled, as did Explorers XVI and XXIII. As previously mentioned, however, the Lunar Orbiter spacecraft were oriented with the large end facing the general direction of the sun.

Neither would this general orientation present a problem had detectors been distributed about the spacecraft in such a way that equal detector areas were exposed to all directions of space throughout the missions. This was not possible because of the small number of detectors flown and of the limited number of positions where detectors could be placed about the spacecraft. As a result of the actual selected arrangement of detectors, the tapered midsection created a 20° half-angle conical blindspot for the detectors about the sun axis. In addition, the solar panels blocked about half of the conical annulus between 20° and 60°. This nonsymmetric look into space was alleviated to some extent by the following factors:

(a) Data were collected continuously from the combined missions for more than one complete orbit around the sun.

(b) The spacecraft were pitched off sun at varying angles throughout their missions.

(c) During the extended missions the spacecraft drifted slowly about the roll axis.

It was possible to obtain an indication of the directionality of the meteoroid flux by determining the approximate position of a detector at the time of penetration. The positions at the times of penetration of only 16 of the 22 punctured detectors could be determined because of roll-gyro problems on Lunar Orbiter II. Some of these positions were obtained by applying known drift rates from times of known spacecraft orientations. The results are presented in figure 5. The circle representing the ring of detectors is shown in a plane perpendicular to the direction of the sun. The top of the ring faces the north ecliptic pole and the right side faces the direction of motion of the earth-moon system around the sun. The approximate position of each detector at the time of penetration is

shown projected upon this plane. These points would be the position of each detector at the moment of penetration if the pitch angle of the spacecraft had been 0^{o}. The actual pitch angles varied from 0^{o} (in at least two cases) to 60^{o} (in possibly one case).

If the ring of detectors in figure 5 is divided in half by a line along the ecliptic poles, 12 of the 16 penetrations were on the side of the spacecraft that faced forward in the orbital direction of the spacecraft movement about the sun. This result agrees with earth-based radar observations reported by Hawkins (ref. 10). Hawkins' data indicate that the influx of meteoroids on the side of the earth facing forward (in orbit about the sun) is several times greater than the influx on the opposite side. (See fig. 6.) Making corrections for the orbital velocity of earth and the average velocity of meteors, Hawkins shows that the apparent directional characteristics of the influx is due to the earth running into meteors on one side and running away from meteors on the opposite side. Although the radar data are for much larger meteoroids than would be required to penetrate the detectors aboard the Lunar Orbiters, the penetration data do show the same general directional trend.

The probability that 12 of 16 penetrations would occur by chance on one side of the spacecraft can be calculated from the expression of the binomial distribution

$$P_n = \frac{N!}{n!(N - n)!} p^n (1 - p)^{N-n} \tag{11}$$

where P_n is the probability that n penetrations will occur on one side out of a total of N penetrations and p is the probability that any one penetration will occur on one side. If it is assumed that approximately the same number of unpunctured detectors are located on either side throughout the missions, then p would be equal to 0.5. For $N = 16$ and $n = 12$, P_n would be equal to 0.03. This result must be multiplied by 2 to obtain the probability that 12 of 16 penetrations could have occurred on either side. Thus, there is a 6-percent chance that the observed distribution of penetrations on Lunar Orbiter spacecraft would have occurred with an apparent omnidirectional flux.

Although the data indicate that the apparent flux might not be omnidirectional, no attempt has been made to determine a correction factor for adjustment of the calculated penetration rate. The angular distribution of meteoroids cannot be established from the data, and directional histories of each detector would be very difficult to determine because of the many spacecraft maneuvers and three-axial drifting. However, it is estimated that the directional preponderance would probably not vary the calculated penetration rate by more than 25 percent. This estimate was determined by computing the differences, as a function of angle, between the directional flux from figure 6 and the omnidirectional flux (calculated from the area within the curves in fig. 6) for the two extreme cases of the spacecraft at pitch angles of $\pm 60^{o}$. The parameter affecting this estimate is the previously mentioned blindspots of the detectors to space.

LUNAR ALTITUDE

Estimates of the flux of secondary meteoroids, or "backsplash," near the moon indicate that it is greater near the lunar surface but drops off sharply with altitude (ref. 11). The estimated velocities of these particles, however, are typically lower than the velocities of primary meteoroids, so that any corresponding penetration hazard, or its variation with altitude, cannot be clearly estimated. The Lunar Orbiter penetration data were therefore examined for indication that the hazard varied with altitude.

To examine the correlation of penetrations with altitude, figure 7 has been plotted to show (1) the percentage of time during lunar orbit that the spacecraft spent at altitude increments of 100 km between perilune and apolune and (2) altitude ranges in which known penetrations occurred. The data were plotted for an orbit ranging from 50 to 1850 km, which was typical of the altitude range where most of the data were obtained. Figure 7 illustrates that a significant part of the orbit time was spent at the low altitudes. A little over 10 percent of the time was spent between 50 and 150 km and approximately one-fourth of the time was spent below an altitude of 500 km.

The entire mission of Lunar Orbiters I, II, and III and part of the Lunar Orbiter V mission were spent in the 50- to 1850-km altitude region. (See table II.) The Lunar Orbiter IV mission and part of the Lunar Orbiter V mission were in polar orbits with an altitude range of 100 to 6200 km. Only eight of the 22 penetrations occurred while the transmitters on the spacecraft were operating continuously; for the remaining 14, the intervals between data readout were so long that the times of penetrations, with the corresponding altitudes, could not be determined. Of these eight penetrations, four occurred while the spacecraft was occulted by the moon. For these four, accordingly, the altitudes at which penetrations occurred can be defined within limits (namely, the highest and lowest altitudes during the occultation periods). The altitudes at which the eight penetrations occurred may then be listed as 305 $\pm$ 120, 360, 810 $\pm$ 90, 1125 $\pm$ 675, 1650, 1685, 5100, and 6040 $\pm$ 100 km. Four of these values show no variation because in each of these cases only 23 seconds elapsed between the telemetered record in which the penetration was first indicated and the previous record. Only the first six are shown in figure 7, since the last two are beyond the limits of the graph.

Study of these data, with due allowance for variation of residence time with altitude (for example, the spacecraft spends less time near perilune than near apolune) failed to indicate any apparent variation of hazard with altitude.

DISCUSSION

The higher meteoroid penetration rates measured near the earth by Explorers XVI and XXIII than near the moon by the Lunar Orbiters could be the result of one or more of

several factors. The most plausible factor, gravitational effects, is discussed subsequently.

First, the small statistical samples of penetrations per Lunar Orbiter spacecraft, as previously discussed, could account for part of this difference. Shielding effects and the directionality of meteoroids can augment the degree of error of the samples. On the other hand, the correlation test has shown good consistency between the penetration data from the five spacecraft.

Second, errors in the calculations of the shielding factors, as discussed in the appendix, could contribute to the differences between the calculated penetration rates near the earth and moon. However, if the differences were due solely to this factor, the effective area would have to be equal to less than 30 percent of the actual surface area of the detectors. By inspection of the geometry, this assumption is untenable.

The uncertainty in the directionality of meteoroids, as discussed previously, is another possible contributor to the difference in the measured rates.

The authors are confident that the differences are not due to limitations of the experiments or the assumptions made in computing the results. It is possible that the differences are real. Temporal variations could account for the real differences in the meteoroid penetration rates. However, this possibility is partly discredited because the two Explorer satellites measured the same penetration rates near the earth over a period of 3 years. This time figure includes a period of 16 months between missions in which no data are available. The time between the end of the meteoroid experiment on Explorer XXIII and the launch of Lunar Orbiter I was 9 months.

The most plausible explanation for the differences could be the influence of gravitational fields on meteoroids. The gravitational field of the earth could affect orbital capture of meteoroids and thereby would tend to increase the near-earth flux above the interplanetary flux. The smaller field of the moon would, of course, capture fewer meteoroids. A discussion of gravitational effects can be found in reference 12. In this reference a gravitational factor G was adopted by applying the work of Öpik (ref. 13). This factor is the ratio of the meteoroid flux near a planet to the flux outside the sphere of influence of a planet and is given by

$$G = 1 + 0.76 \frac{R_p V_p^2 r_p}{V_e^2 r_s} \tag{12}$$

where

r_p radius of planet

r_s distance from planet's center

R_p distance of planet from sun in astronomical units

V_e escape velocity from earth's surface

V_p escape velocity from planet's surface

For Explorers XVI and XXIII, G is equal to 1.66. If this value is divided into the measured Explorer rates of 0.44 and 0.48 m^{-2}-day^{-1}, as calculated previously, the meteoroid penetration rates away from the gravitational influence of the earth become 0.27 and 0.29 m^{-2}-day^{-1} for Explorers XVI and XXIII, respectively. These values, obviously, agree more closely with the Lunar Orbiter rate of 0.18 m^{-2}-day^{-1}, which has been corrected by a factor G of 1.036.

Based on their analyses and confidence in the validity of the experiments, the authors believe that the measured difference in the penetration rates near the earth and moon is real; less confidence is placed upon the exact magnitude of the difference. More experimentation is required before this question can be resolved. At this time it appears reasonable to assume that the meteoroid hazard near the moon is no greater and very possibly less than the hazard near the earth.

CONCLUSIONS

The meteoroid penetration experiments on the Lunar Orbiter in the altitude range of 30 to 6200 km above the lunar surface indicate an average penetration rate of 0.16 m^{-2}-day^{-1} in 0.025-mm-thick beryllium copper, which was less than one-half the rate measured in the near-earth environment by Explorers XVI and XXIII. Analytical tests indicate good consistency of the data from each of the five Lunar Orbiter experiments.

Individual penetrations were examined to detect directionality and altitude effects on the measurements. The directionality dependence appeared to be in good agreement with that shown by earth-based radar observations. There was no apparent altitude dependence, and the data did not show evidence of an increase in the hazard, such as might result from a large secondary flux ("backsplash" from impacts of primary meteoroids on the lunar surface) in the altitude range of 30 to 6200 km.

The difference between the penetration rates near the moon and near the earth could be the result of several factors such as gravitational distortions or temporal variations in the meteoroid flux. From the results presented in this report, it can be stated

with good confidence that the penetration hazard for 0.025-mm-thick beryllium-copper near the moon is no greater and probably less than the hazard near the earth.

Langley Research Center,
National Aeronautics and Space Administration,
Hampton, Va., April 19, 1971.

APPENDIX

CALCULATION OF THE EFFECTIVE AREA OF THE METEOROID EXPERIMENT

In determining the penetration or flux rates of meteoroids in space, careful attention must be allocated to the geometry of the meteoroid sensors on the spacecraft. Two basic parameters of the geometry that must be considered are the shape of the sensitive surface and the unshielded look angle of the sensors. Different bodies, spacecraft, and sensors will receive meteoroid impacts whose number will be dependent on time, area, the degree of self-shielding, and the degree of shielding from other bodies. To predict the flux that a spacecraft would receive during its mission, the flux rate as measured by experiment must be given in terms of values of the sensor configuration that can be readily applied to the spacecraft configuration. The calculations can be accomplished by use of the parameter of "effective area" as defined in the following paragraphs.

Definitions

Before proceeding with the calculations of the effective areas of the sensors, several terms require definition.

Regular body – a body having a surface that cannot be penetrated more than twice by a straight line

Shielded body – a body that is partially or wholly shielded from space by another body or by parts of itself (as in the case of an irregular body)

Projected area (A_p) – the area of a body as seen from a point in space (The projected area of a surface element dA of a body is given by $dA \cos \theta$, where θ is the viewing angle from the normal of dA.)

Average projected area $(\overline{A}_p)$ – the projected area of a body averaged over all possible orientations in space

Effective area (A_e) – the effective area of the surface of any body is a value that is calculated to take into account the reduction in the exposure to space of the body as a result of shielding factors (In other words, this calculation is a means of equating the exposures to space of shielded and unshielded surfaces of bodies.)

The effective area of the meteoroid experiment is a key parameter required to determine the meteoroid penetration rate. The effective area of a shielded body is less than its actual surface area. For an irregular body, some external surface elements of the body are shielded from space by other elements of its own surface. This

self-shielding effect reduces the maximum possible exposure of the surface to space. Thus, the average projected area and the effective area of the body are reduced. In essence, the effective area for this case is a means of equating irregular bodies to regular bodies. For these definitions, a doughnut is a good example of an irregular body.

The surface areas of the test material on the pressurized-cell detectors are regular surfaces with half-cylinder configurations. However, these surfaces are shielded from certain directions in space by parts of the spacecraft, such as, the solar panels and antennas. Also the detectors in each set of five side-by-side detectors (hereafter referred to as double detectors) partially shield each other. Thus, the effective area of the detectors must be calculated to equate their areas to unshielded regular detectors.

Effective Area

The effective area of a surface can be calculated from the average projected area. The calculation of the average projected area of any regular body is straightforward. Consider an element of area dA whose vector $\overrightarrow{dA}$ is normal to the surface element. The average of the projected surface elements over all space is given by

$$\overline{dA_p} = \frac{\iint \left| \overrightarrow{dA} \cdot \overrightarrow{dw} \right|}{\iint dw} \tag{A1}$$

where dw is an element of solid angle. Since the total solid angle is 4π, equation (A1) becomes

$$\overline{dA_p} = \frac{1}{4\pi} \iint \left| \overrightarrow{dA} \cdot \overrightarrow{dw} \right| \tag{A2}$$

In spherical coordinates, equation (A2) can be written as

$$\overline{dA_p} = \frac{dA}{4\pi} \int_{\theta_1}^{\theta_2} \int_{\phi_1}^{\phi_2} \cos\theta \sin^2\phi \, d\theta \, d\phi \tag{A3}$$

Integration of equation (A3) leads to the result

$$\overline{dA_p} = \frac{1}{4} dA \tag{A4}$$

By integrating both sides, equation (A4) becomes

$$\overline{A_p} = \frac{1}{4} A \tag{A5}$$

where A is the actual surface area of a regular body. A more complete discussion of this result can be found in reference 14.

Consider a sphere, a regular body, which has a surface area of $4\pi r^2$, where r is the radius. By equation (A5) the average projected area of the sphere is equal to πr^2. For this particular case, this is also equal to the projected area of the sphere as seen from any direction in space. Moreover, the effective area is equal to the actual area $4\pi r^2$ since it is a regular body. From the definitions given above and from equation (A5), the effective area of any body is given by

$$A_e = 4\overline{A}_p \tag{A6}$$

The determination of the average projected area of the test material of the meteoroid detectors on the Lunar Orbiter spacecraft will comprise the rest of this appendix.

Detector-Spacecraft Configuration

Figure 8 shows a drawing of the spacecraft as viewed from the top. The location of the main row of 15 detectors is shown. Immediately evident are three differently positioned detectors, labeled A, B, and C, relative to the solar panels. Type A is centered in front of a solar panel, type B is centered between two solar panels, and type C is centered between A and B. To simplify the calculations, it was assumed that each detector lies on a fixed radius from the center of the spacecraft in the Y-Z plane and that the detectors are spaced 22.5° apart. As will be pointed out, the exact spacing is not important.

The calculations of the average projected area of each detector were further complicated by the five sets of double detectors, indicated in figure 8 by the "x" on the lower detector of each set. As a result, separate calculations were made for six different cases as designated in table VI. For example, case III consists of three detectors of type B, each being in the lower row of a set of double detectors. In some instances, parts of the calculations for one case could be applied to another case.

To simplify the calculations one step further, it was assumed that the base of the spacecraft was shaped as shown in figure 9. Most of the apparent exposed area lost in the vicinity of the junction of the solar panels is actually lost due to the shielding by spacecraft components. The area loss at the outer corners of the solar panels is small.

Basic Equation for Determination of Average Area

Consider a vector $\overrightarrow{dA}$ drawn normal to the surface element dA on the test material of a detector. Figure 10 represents a cross-sectional view of a detector. The rectangular coordinate system is defined as shown in the figure with the Z-axis normal to the page. If α is the angle between $\overrightarrow{dA}$ and the X-axis, then the general form of the integral of $\overline{dA}_\alpha$ from equation (A3) is given by

$$\overline{dA}_\alpha = \frac{dA_\alpha}{4\pi} \int_{\theta_1}^{\theta_2} \int_{\phi_1}^{\phi_2} \cos(\theta - \alpha)\sin^2\phi \, d\theta \, d\phi \tag{A7}$$

where the limits of integration depend upon the shielding geometry as seen from the surface element. The spherical coordinates are defined as shown in figure 11.

Since the test material is symmetric about the Z-axis, the average of $\overline{dA}_\alpha$ for α between 0 and π is equal to the average projected area $\overline{dA}_p$ of all the area elements of the test material as given by

$$\overline{dA}_p = \frac{\int_{\alpha_1}^{\alpha_2} \overline{dA}_\alpha \, d\alpha}{\int_0^\pi d\alpha} \tag{A8}$$

or

$$\overline{dA}_p = \frac{1}{\pi} \int_{\alpha_1}^{\alpha_2} \overline{dA}_\alpha \, d\alpha \tag{A9}$$

Substituting equation (A7) into equation (A9) yields

$$\overline{dA}_p = \frac{dA}{4\pi^2} \int_{\alpha_1}^{\alpha_2} \int_{\theta_1}^{\theta_2} \int_{\phi_1}^{\phi_2} \cos(\theta - \alpha)\sin^2\phi \, d\alpha \, d\theta \, d\phi \tag{A10}$$

If A is the total area of the test-material surface, then

$$\overline{A}_p = \frac{A}{4\pi^2} \int_{\alpha_1}^{\alpha_2} \int_{\theta_1}^{\theta_2} \int_{\phi_1}^{\phi_2} \cos(\theta - \alpha)\sin^2\phi \, d\alpha \, d\theta \, d\phi \tag{A11}$$

This equation is used in determining the average projected area of all the meteoroid detectors. The limits of integration must be determined for all six cases. (See table VI.)

Case I

Case I, a single detector centered above a solar panel, is the simplest case and the basis on which all the other cases were considered. Figure 12(a) represents the geometry. The $y = 0$ plane and the panel area CDFG are the areas that shield the test material from space. A cross-sectional view ($z = 0$) is shown in figure 12(b). The figure is divided into four regions of integration. These regions are dependent upon the limits of the angle θ as a function of the angle α. Region 4 is distinguished to separate the regions of no shielding and the region of partial shielding due to the solar panel. The separation is made at $\pi - \omega$, the angle between the positive X-axis and the line drawn to the outer edge

of the solar panel in the $z = 0$ plane. Table VII shows the variation of θ, shielded and unshielded, as a function of the variation of α.

In regions 1, 2, and 3 the boundaries of ϕ are 0 and π. The boundaries of ϕ in region 4 are determined by the planes AGF and ACD as shown in figure 12(a). The equation of the plane AGF was found by solving the equation

$$b_1x + b_2y + b_3z = b_4 \tag{A12}$$

for the three points (0,0,0), (-a,0,c), and (-a,d,c) with the result

$$az + cx = 0 \tag{A13}$$

Transformation to spherical coordinates yields

$$\tan \phi = -\frac{a}{c} \sec \theta \tag{A14}$$

Thus, one limit of integration of ϕ is given by

$$\phi = \tan^{-1}\left(-\frac{a}{c} \sec \theta\right) \tag{A15}$$

By the same procedure the other limit was found to be

$$\phi = \tan^{-1}\left(+\frac{a}{c} \sec \theta\right) \tag{A16}$$

By applying equations (A15) and (A16) and the limits in table VII, the average projected area of the test material for case I detectors is given by

$$\overline{A}_p = \frac{A}{4\pi^2}\left[\int_0^{\frac{\pi}{2}-\omega}\int_0^{\alpha+\frac{\pi}{2}}\int_0^{\pi} f(\gamma)d\gamma + \int_{\frac{\pi}{2}-\omega}^{\pi/2}\int_0^{\pi-\omega}\int_0^{\pi} f(\gamma)d\gamma\right.$$

$$+ \int_{\pi/2}^{\pi}\int_{\alpha-\frac{\pi}{2}}^{\pi-\omega}\int_0^{\pi} f(\gamma)d\gamma + 2\int_{\frac{\pi}{2}-\omega}^{\pi/2}\int_{\pi-\omega}^{\alpha+\frac{\pi}{2}}\int_0^{\tan^{-1}\left(-\frac{a}{c}\sec\theta\right)} f(\gamma)d\gamma$$

$$\left. + 2\int_{\pi/2}^{\pi}\int_{\pi-\omega}^{\pi}\int_0^{\tan^{-1}\left(-\frac{a}{c}\sec\theta\right)} f(\gamma)d\gamma\right] \tag{A17}$$

where

$$f(\gamma)d\gamma = \cos(\theta - \alpha)\sin^2\phi \, d\alpha \, d\theta \, d\phi \tag{A18}$$

The integration of the first three integrals is straightforward; the last two integrals were solved on a computer. As a result, for case I detectors,

$$\overline{A}_p = 0.174A \tag{A19}$$

By equation (A5) the effective area is

$$A_e = 4\bar{A}_p = 0.696A \tag{A20}$$

Since A is equal to 0.014 m^2,

$$A_e = 0.00974 \text{ m}^2 \tag{A21}$$

Thus, the shielding of the thermal blanket and solar panels on case I detectors resulted in a loss of about 30 percent of the effective area.

Transformation Equations

To find the equations for the geometry, shielding boundaries, and limits of integration for type B and C detectors, a translation and a rotation must be performed on the type A (case I) detector coordinate system. The transformed axes are shown in figure 13. If the coordinate system is translated along the circumference of the circle of radius r through an angle σ, the transformation equations are given by

$$\left.\begin{aligned} y &= y' - k_1 \\ z &= z' + k_2 \end{aligned}\right\} \tag{A22}$$

Then the coordinate system is rotated to an angle σ. This transformation is given by

$$\left.\begin{aligned} y' &= y'' \cos\sigma - z'' \sin\sigma \\ z' &= y'' \sin\sigma + z'' \cos\sigma \end{aligned}\right\} \tag{A23}$$

By combining equations (A22) and (A23), the transformation from (y,z) to (y'',z'') is given by

$$\left.\begin{aligned} y &= y'' \cos\sigma - z'' \sin\sigma - k_1 \\ z &= y'' \sin\sigma + z'' \cos\sigma + k_2 \end{aligned}\right\} \tag{A24}$$

As indicated previously for type B and C detectors, σ is equal to 45° and 22.5°, respectively. It should be noted that the transformation equations would be different if the rotation was performed before the translation. However, the transformed parameters would be the same by either method.

Double-Detector Boundary Equations

Some of the type B and C detectors involve sets of double detectors. Consider the case of the lower detector shielding the upper detector from space. In figure 14 the angle κ must be determined at point D on the upper detector. This is the largest angle for a given angle α in which an element of area dA at D is not shielded by the lower detector. The angle κ can be found through the equation

$$\kappa = \pi - \epsilon = \beta + \Delta + \frac{\pi}{2} \tag{A25}$$

The angles β and Δ are given by

$$\beta = \sin^{-1} \frac{BC}{CD} \tag{A26}$$

and

$$\Delta = \sin^{-1} \frac{r}{CD} \tag{A27}$$

The line BC can be written

$$\begin{aligned} BC &= AC - AB \\ &= 2r - r\cos(\pi - \alpha) \\ &= 2r + r\cos\alpha \end{aligned} \tag{A28}$$

Also,

$$\begin{aligned} CD &= \left[(BC)^2 + (BD)^2\right]^{1/2} \\ &= \left[(2r + r\cos\alpha)^2 + (r\sin\alpha)^2\right]^{1/2} \\ &= \left(4r^2 + 4r^2\cos\alpha + r^2\cos^2\alpha + r^2\sin^2\alpha\right)^{1/2} \\ &= r(4 + 4\cos\alpha + 1)^{1/2} \\ &= r(5 + 4\cos\alpha)^{1/2} \end{aligned} \tag{A29}$$

Combining equations (A25) to (A29) yields

$$\kappa = \sin^{-1}\left[\frac{2 + \cos\alpha}{(5 + 4\cos\alpha)^{1/2}}\right] + \sin^{-1}\left[\frac{1}{(5 + 4\cos\alpha)^{1/2}}\right] + \frac{\pi}{2} \tag{A30}$$

The angle κ is an upper limit of integration for determining the average projected area of an upper detector. For the lower detector, the corresponding lower limit of integration was found by the same procedure to be

$$\kappa = \sin^{-1}\left[\frac{2 - \cos\alpha}{(5 - 4\cos\alpha)^{1/2}}\right] + \sin^{-1}\left[\frac{1}{(5 - 4\cos\alpha)^{1/2}}\right] - \frac{\pi}{2} \tag{A31}$$

Case V

By applying the transformation and double-detector equations, the average projected areas for cases II to VI can be found by the procedures used for case I. Discussion of the details of each case would require many pages. As an example, the most complicated case, case V, will be briefly discussed. Case V involves an upper detector of a set of double detectors located asymmetrically with respect to the solar panels and 22.5° from case I detectors. (See fig. 15.)

By using the same procedure as in case I, regions of integration were defined. In figure 15 the dashed lines which intersect the corners of the solar panels divide the regions for α greater than $\pi - \omega$. Figure 16 shows in the X-Y plane all 10 regions required for the calculation of the average projected area. The limits of integration of ϕ as defined by the five edges of the exposed solar panels were found to be given by the general equation (see procedure for eq. (A15))

$$\phi = \tan^{-1}\left(\frac{1}{S_1 \sin\theta + S_2 \cos\theta}\right) \tag{A32}$$

where S_1 and S_2 are constants that are different for each edge.

The calculation of the average projected area for this case required 29 integrals, 25 of which were solved on a computer. The value was found to be

$$\bar{A}_p = 0.166A \tag{A33}$$

and the effective area is, therefore, equal to

$$A_e = 0.0093\ m^2 \tag{A34}$$

Results

The values of the average projected areas for the six cases of detector-spacecraft configurations are given in table VIII. The effective areas are calculated from equation (A6). Obviously there is a duplication of values. All the single detectors around the support ring on the spacecraft have the same effective area. This is true for the upper detectors and the lower detectors of the sets of double detectors. As a result, the cases can be reclassified as shown in table IX. This result is surprising, since the projected area of a detector as seen from any element of solid angle is a cosine function. Apparently the variation of the position of the solar panels with respect to the detectors is compensated by the variation of the exposed panel area.

As previously mentioned, 30 percent of the effective area of the single detector is lost because of the spacecraft configuration. However, it was calculated that 18 percent of the loss was due to the shielding of the $y = 0$ plane, with the remaining 12 percent

due to the solar panels. This result applies also to the double detectors. It may at first seem surprising that the effective areas of the single and double detectors are only slightly different. Calculations were performed to determine the effective-area loss of one double detector due only to the shielding of the other detector. Only half of the surface area of the detector is affected by this shielding. The effective-area loss over this area was found to be about 36 percent. Since 18 percent of the effective-area loss would be lost anyhow due to the shielding of the $y = 0$ plane as for the single detector, the difference between the single and double detectors amounts to an 18-percent area loss of half of the detector surface or 9 percent of the total detector area. This is equivalent to a maximum difference of 13 percent between the effective area of the detectors. This difference is less for the upper detectors since some of the area lost by this detector because of the lower detector shielding is already lost in the case of the single detector because of solar-panel shielding.

In performing the calculations of the effective area of the detectors, certain factors were neglected. Some of these factors were

(a) Irregularities in the thermal blanket

(b) Shape of the test material from a true semicylinder

(c) Different values of the angle ω for each solar panel

(d) Area shielded by the antennas

(e) Penetrations resulting from secondary ejecta of meteoroids hitting other parts of the spacecraft, and

(f) The angle of incidence of the meteoroid on the detector surface

Irregularities in the thermal blanket are mainly bulges due to the camera canister and fuel tanks. The first three factors are considered to be very small variations. The area lost from the small-antenna shielding is also very small. Calculations were made on the area lost because of the large high-gain antenna. The calculations were complicated by the fact that this antenna rotates with a 1-month period. The position for maximum shielding results in an area loss of 4 percent for the detectors in front of the antenna. Considering the low flux rates encountered by Lunar Orbiter spacecraft, the probability of occurrence of (e) would be small. Moreover, most of the spacecraft surface about the detectors is the thermal blanket which can readily be penetrated by meteoroids. As for (f), all meteoroids that penetrate the test material through the surface of the double detectors near the intersection of the two detectors have large angles of incidence. As a result, a weighting factor as a function of average angle of incidence should be placed on each surface element. These weighting factors cannot be determined since the size, mass, and velocity distributions of the meteoroids are unknown. The uncertainties (a) through (f) are not large compared with the statistical uncertainty in determining the

true mean penetration rate from the small number of penetrations that occurred during the experiments.

The value of 0.186 m^2 is adopted from table IX as the total effective area of the 20 detectors on each spacecraft. The effective area of any detector is considered to be 0.0093 m^2. This value is within 10 percent of the values determined for the six cases. (A 10-percent error would arise only if all the penetrations occurred in the single or double-bottom detector, as designated in table IX. Actually, the 22 penetrations were distributed in such a manner that the error in the area loss amounts to 0.48 percent.)

REFERENCES

1. Nazarova, T. N.; Rybakov, A. K.; and Komissarov, C. D.: Investigations of Solid Interplanetary Matter in the Vicinity of the Moon. Paper presented at 10th Plenary Meeting of COSPAR (London, England), July 1967.

2. Hastings, Earl C., Jr., compiler: The Explorer XVI Micrometeoroid Satellite – Supplement III, Preliminary Results for the Period May 27, 1963, Through July 22, 1963. NASA TM X-949, 1964.

3. O'Neal, Robert L., compiler: The Explorer XXIII Micrometeoroid Satellite – Description and Preliminary Results for the Period November 6, 1964, Through February 15, 1965. NASA TM X-1123, 1965.

4. Whipple, Fred L.: On Meteoroids and Penetration. J. Geophys. Res., vol. 68, no. 17, Sept. 1963, pp. 4929-4939.

5. Konstantinov, B. P.; Bredov, M. M.; and Mazets, E. P.: Experimental Evidence Against the Hypothesis of an Earth Dust Cloud. Proc. Acad. Sci. (USSR), vol. 174, May 21, 1967, pp. 580-582.

6. Nilsson, C.: Some Doubts About the Earth's Dust Cloud. Science, vol. 153, no. 3741, Sept. 9, 1966, pp. 1242-1246.

7. Hogg, Robert V.; and Craig, Allen T.: Introduction to Mathematical Statistics. Second ed., Macmillan Co., c.1965, pp. 243-246.

8. Young, Hugh D.: Statistical Treatment of Experimental Data. McGraw-Hill Book Co., Inc., c.1962, pp. 101-132.

9. Burington, Richard Stevens; and May, Donald Curtis, Jr.: Handbook of Probability and Statistics With Tables. Handbook Publ., Inc. (Sandusky, Ohio), c.1953, pp. 116-133. (Reprinted 1958.)

10. Hawkins, Gerald S.: A Radio Echo Survey of Sporadic Meteor Radiants. Monthly Notice, Rep. Astronomical Soc., vol. 116, no. 1, 1956, pp. 92-104.

11. Gault, Donald E.; Shoemaker, Eugene M.; and Moore, Henry J.: Spray Ejected From the Lunar Surface by Meteoroid Impact. NASA TN D-1767, 1963.

12. Anon.: Meteoroid Environment Model – 1970 [Interplanetary and Planetary]. NASA Space Vehicle Design Criteria (Environment). NASA SP-8038, 1970.

13. Öpik, E. J.: Collision Probabilities With the Planets and the Distribution of Interplanetary Matter. Proc. Roy. Irish Acad., vol. 54A, 1951, pp. 165-199.

14. Vouk, V.: Projected Area of Convex Bodies. Nature, vol. 162, no. 4113, Aug. 28, 1948, pp. 330-331.

TABLE I.- LUNAR ORBITER LAUNCH AND IMPACT DATES

Lunar Orbiter	Launch	Lunar impact
I	August 10, 1966	October 29, 1966
II	November 6, 1966	October 11, 1967
III	February 4, 1967	October 9, 1967
IV	May 4, 1967	October 1967[a]
V	August 2, 1967	January 31, 1968

[a]Telemetry lost on July 17, 1967.

TABLE II.- ORBITAL PARAMETERS FOR SPACECRAFT

Lunar Orbiter	Parameter	Lunar injection	Orbit change				
			1	2	3	4	5
I	Date	8-14-66	8-21-66	8-25-66	10-29-66		
	Perilune, km	198	54	43	0		
	Apolune, km	1857	1855	1827			
	Inclination, deg	12.1	12.1	12.1	Impact		
II	Date	11-10-66	11-15-66	12-8-66	4-14-67	6-27-67	10-11-67
	Perilune, km	205	39	54	66	115	0
	Apolune, km	1863	1863	1871	1840	1841	
	Inclination, deg	12.0	11.9	17.5	16.9	16.6	Impact
III	Date	2-8-67	2-12-67	4-12-67	7-17-67	8-30-67	10-9-67
	Perilune, km	213	52	55	143	123	0
	Apolune, km	1799	1849	1825	1824	340	
	Inclination, deg	20.9	21.0	21.0	21.0	21.3	Impact
IV	Date	5-8-67	6-5-67	6-8-67	7-17-67		
	Perilune, km	2651	76	70	Lost		
	Apolune, km	6172	6089	3958			
	Inclination, deg	85.3	84.8	84.8			
V	Date	8-5-67	8-7-67	8-9-67	10-10-67	1-31-68	
	Perilune, km	196	100	98	200	Impact	
	Apolune, km	6029	6060	1503	1986		
	Inclination, deg	84.9	84.6	84.7	85.1		

TABLE III.- METEOROID PENETRATION HISTORIES

Penetration	Lunar Orbiter[a]				First record date (G.m.t.), yr-day-hr	Time since last readout, hours
	II	III	IV	V		
1	1				66-319-13	23 sec
2	2				66-329-17	1
3	3				66-338-02	23 sec
4	4				67-006-20	0.1
5		1			67-089-12	49
6		2			67-111-12	19
7	5				67-116-07	36
8			1		67-132-02	23 sec
9			2		67-139-00	2
10	6				67-167-21	45
11	7				67-171-02	49
12	8				67-209-08	81
13				1	67-221-05	23 sec
14		3			67-230-02	55
15	9				67-258-20	47
16				2	67-264-08	46
17		4			67-267-18	57
18	10				67-267-20	78
19				3	67-320-18	32
20				4	67-325-03	0.5
21				5	67-361-05	120
22				6	68-021-07	65

[a]Lunar Orbiter I had no penetrations.

TABLE IV.- PENETRATIONS AND TIME-AREA PRODUCTS

Lunar Orbiter	Number of penetrations	Time-area, m^2-day
I	0	14.1
II	10	45.8
III	4	38.8
IV	2	11.8
V	6	28.5
Total	22	139.0

TABLE V.- METEOROID DATA FROM LUNAR ORBITERS AND EXPLORERS XVI AND XXIII

Spacecraft	Penetrations	Time-area exposure, m^2-days	Penetration rate, penetrations/m^2-day
Lunar Orbiters I to V	22	139.0	0.16
Explorer XVI	44	132.9	.33
Explorer XXIII	50	139.9	.36

TABLE VI.- CLASSIFICATION OF DETECTORS BASED ON DIFFERENT SHIELDING CONFIGURATIONS[a]

Case	Type	Single or double	Upper or lower	Number of detectors
I	A	Single		4
II	B	Double	Upper	3
III	B	Double	Lower	3
IV	C	Single		6
V	C	Double	Upper	2
VI	C	Double	Lower	2

[a]Shielding configurations were identical for all Lunar Orbiter spacecraft.

TABLE VII.- VARIATION OF ANGLE θ FOR GIVEN ANGLE α RANGE

Region of integration	Limits of α, rad		Limits of θ, rad, for –			
			Unshielded ($0 \leq \phi \leq \pi$)		Partially shielded	
	Lower	Upper	Lower	Upper	Lower	Upper
1	0	$\frac{\pi}{2} - \omega$	0	$\alpha + \frac{\pi}{2}$	-----	-----
2	$\frac{\pi}{2} - \omega$	$\frac{\pi}{2}$	0	$\pi - \omega$	-----	-----
3	$\frac{\pi}{2}$	$\pi - \omega$	$\alpha - \frac{\pi}{2}$	$\pi - \omega$	$\pi - \omega$	$\alpha + \frac{\pi}{2}$
4	$\pi - \omega$	π	$\alpha - \frac{\pi}{2}$	$\pi - \omega$	$\pi - \omega$	π

TABLE VIII.- EFFECTIVE AREA OF DETECTORS FOR THE SIX CASES

Case	$\overline{A}_p/A$	A_e, m^2
I	0.174	0.00974
II	.166	.00930
III	.150	.00840
IV	.174	.00974
V	.166	.00930
VI	.150	.00840

TABLE IX.- EFFECTIVE AREAS AND TOTAL AREAS WITH DETECTOR TYPES RECLASSIFIED

Detector type	A_e, m^2	Number of detectors	Total effective area, m^2
Single	0.00974	10	0.0974
Double-top	0.00930	5	0.0465
Double-bottom	0.00840	5	0.0420
Total			0.1859

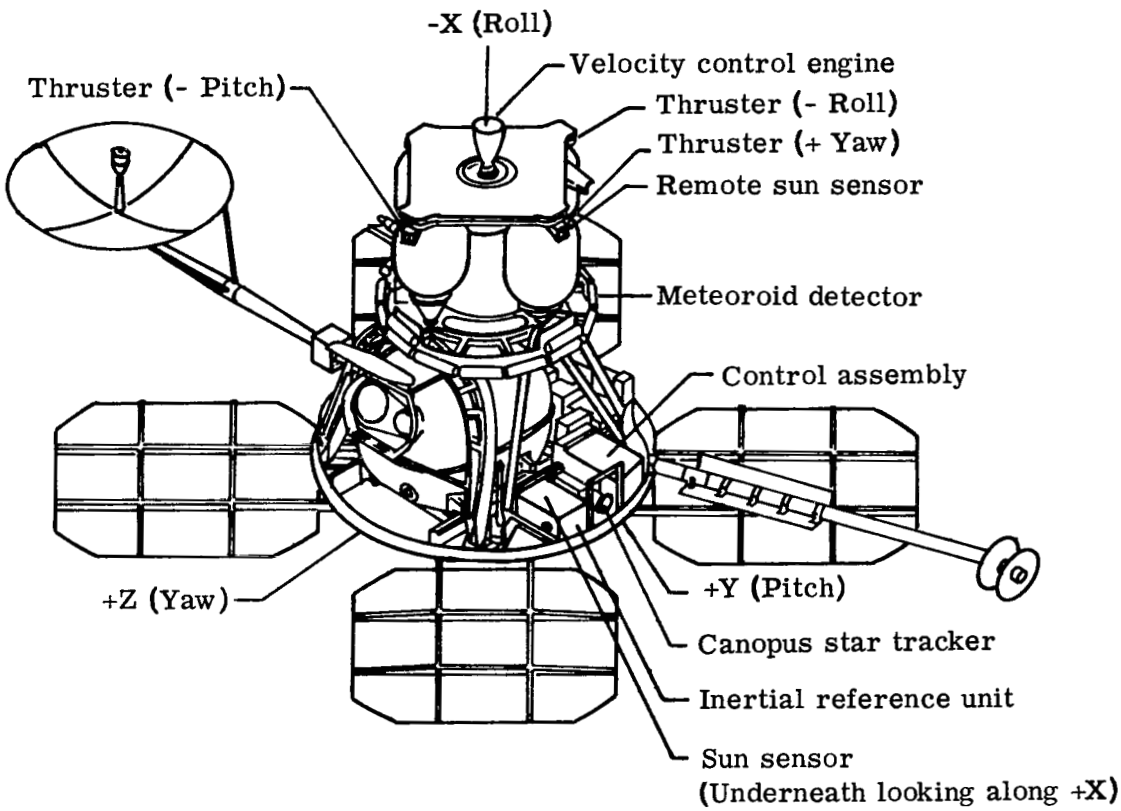

Figure 1.- Attitude control subsystem components and axial orientation.

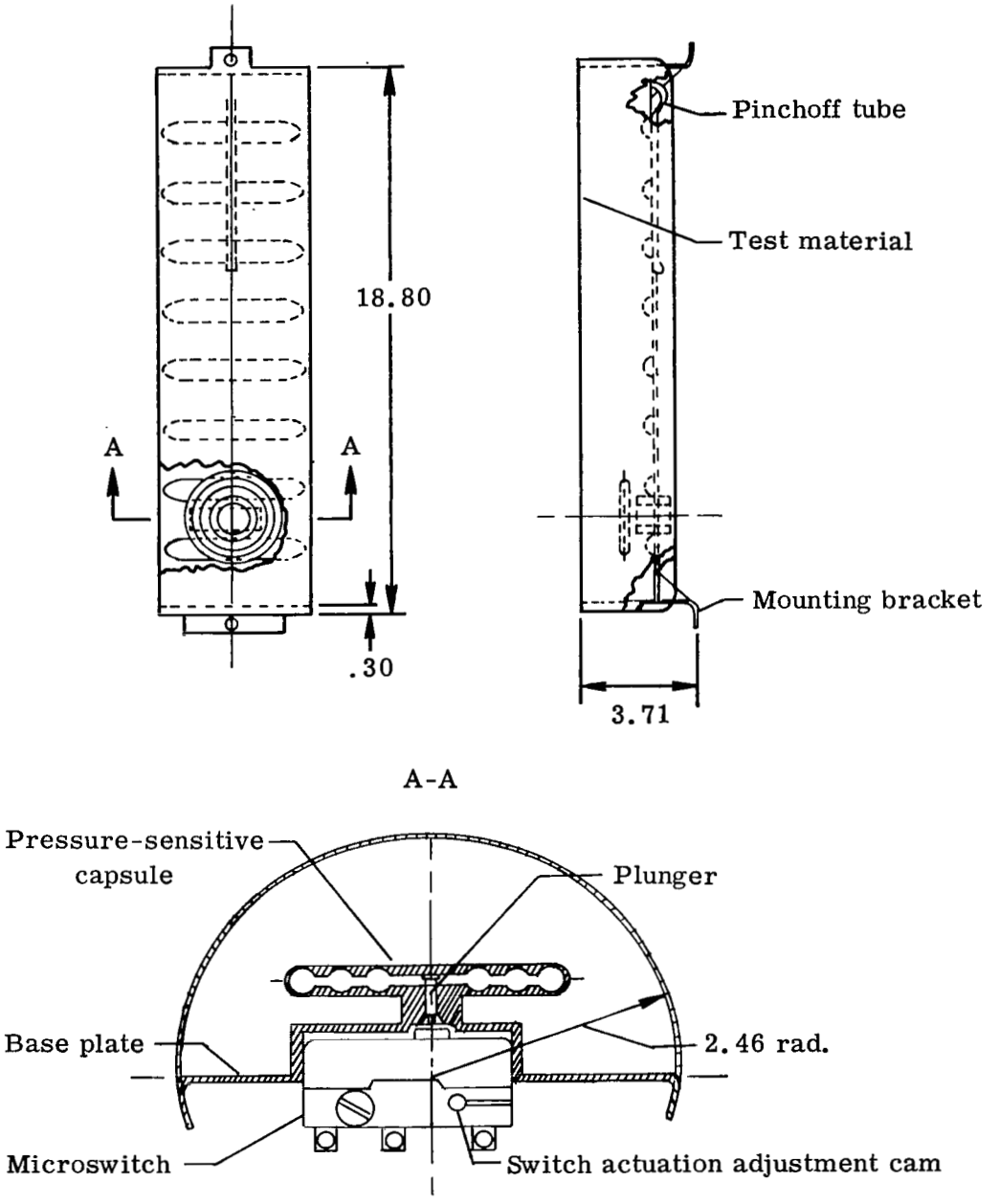

Figure 2.- Pressurized-cell meteoroid detector. All dimensions are in centimeters.

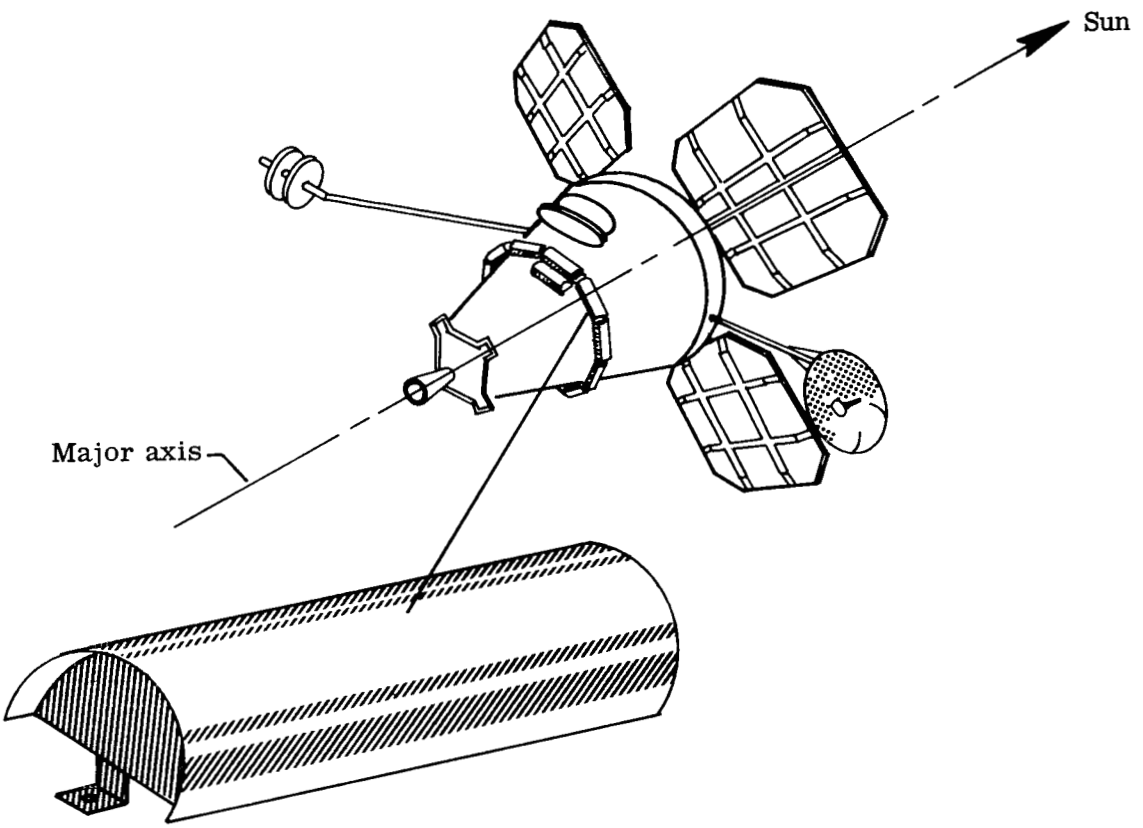

Figure 3.- Geometry of meteoroid detectors on spacecraft.

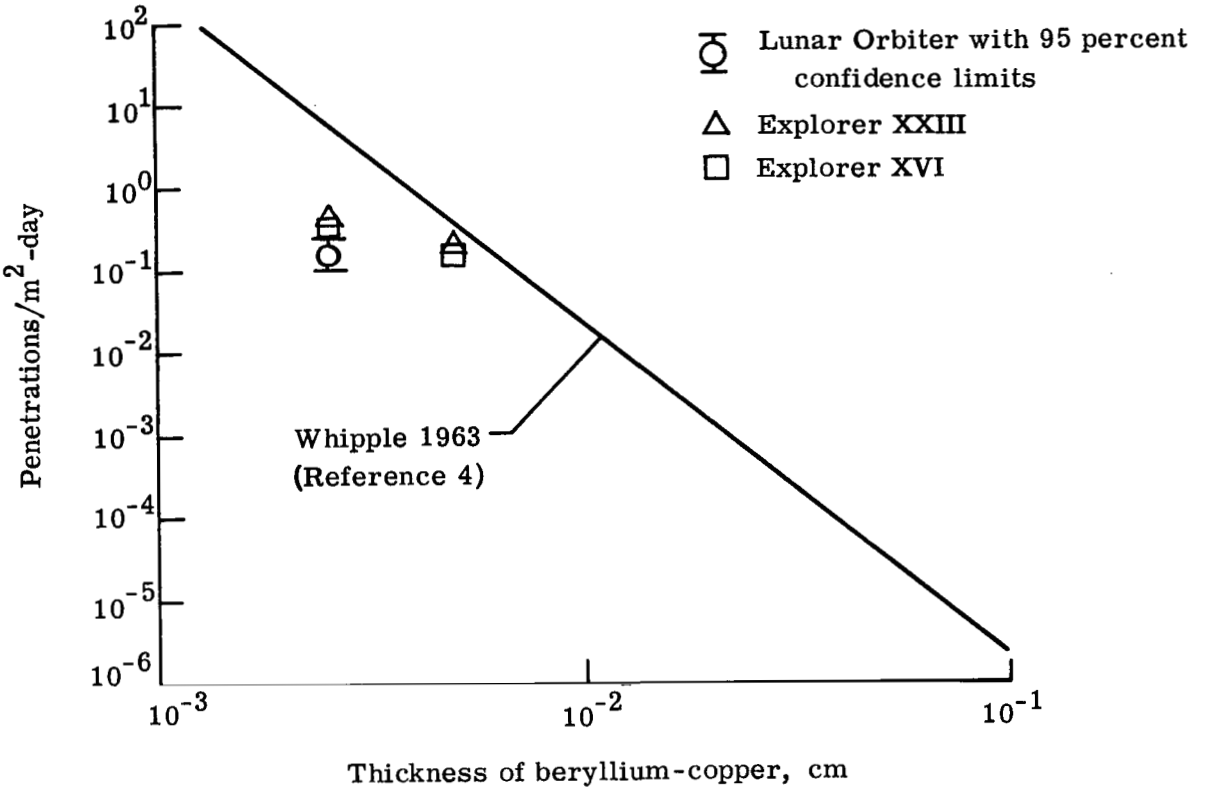

Figure 4.- Penetration rates for beryllium-copper pressurized-cell detectors on Lunar Orbiter and Explorers XVI and XXIII and comparison with Whipple's 1963 prediction converted to beryllium-copper. (The Explorers carried both 0.025- and 0.050-mm-thick beryllium-copper meteoroid detectors.)

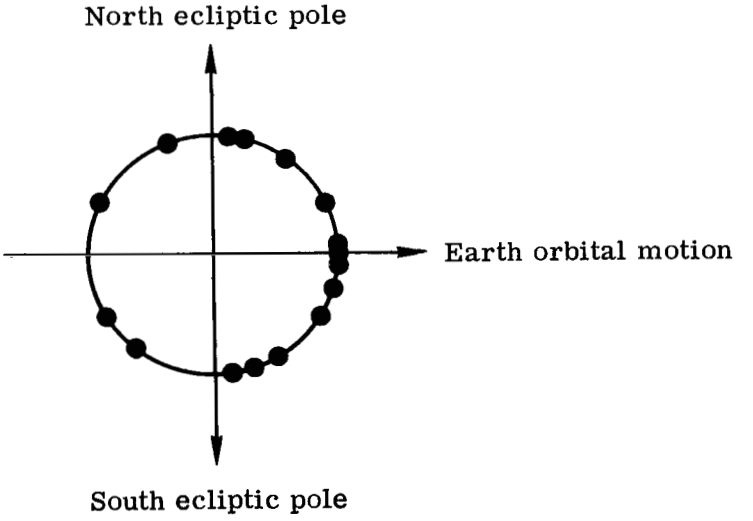

Figure 5.- Cross-sectional representation of ring of detectors showing position of detectors during times of penetration.

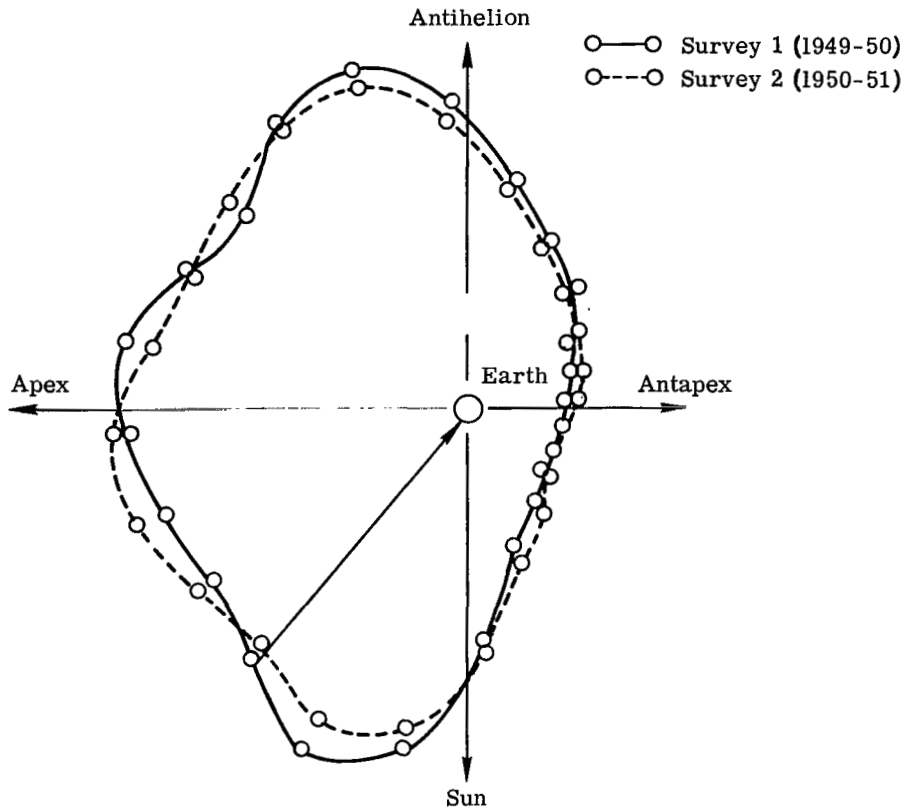

Figure 6.- Polar diagram drawn in plane of earth's orbit, which shows apparent number of meteoroids per unit angle per unit time (taken from ref. 10).

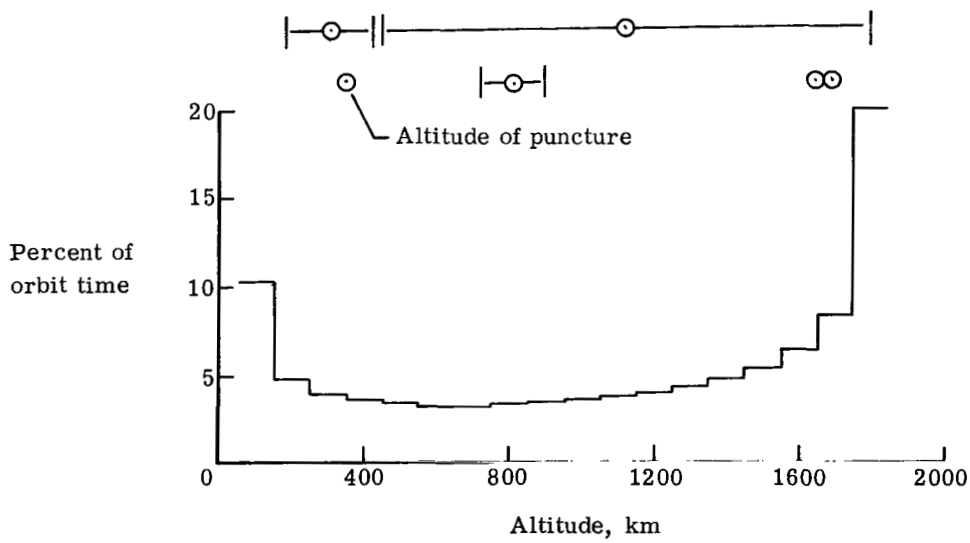

Figure 7.- Percent of orbit time as a function of 100-km increments of altitude above lunar surface. Spacecraft altitude at times of penetration is shown with uncertainty bars except where altitude was accurately known.

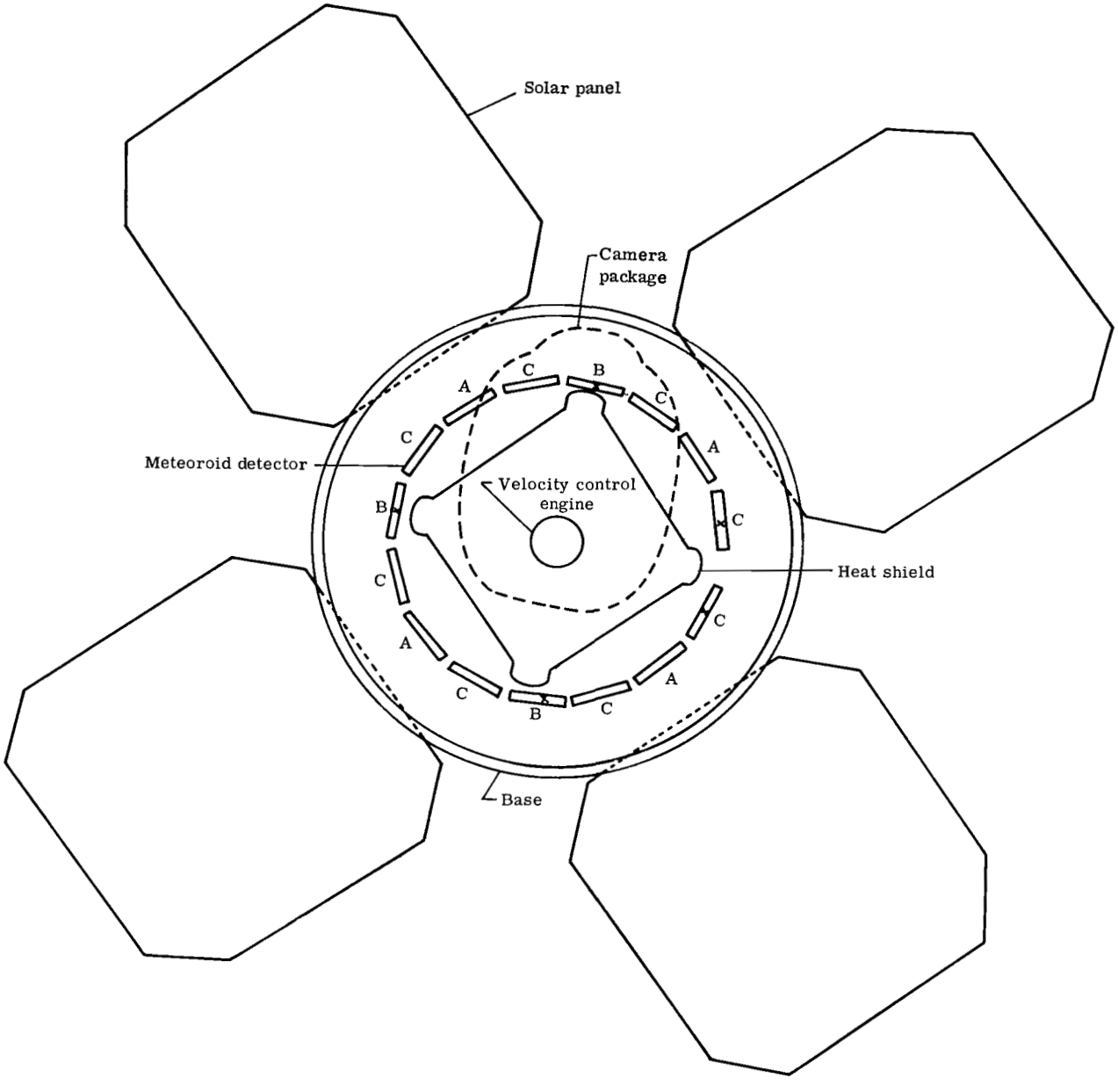

Figure 8.- View of detectors on spacecraft from small end, with types A, B, and C detectors designated and double detectors indicated by "x."

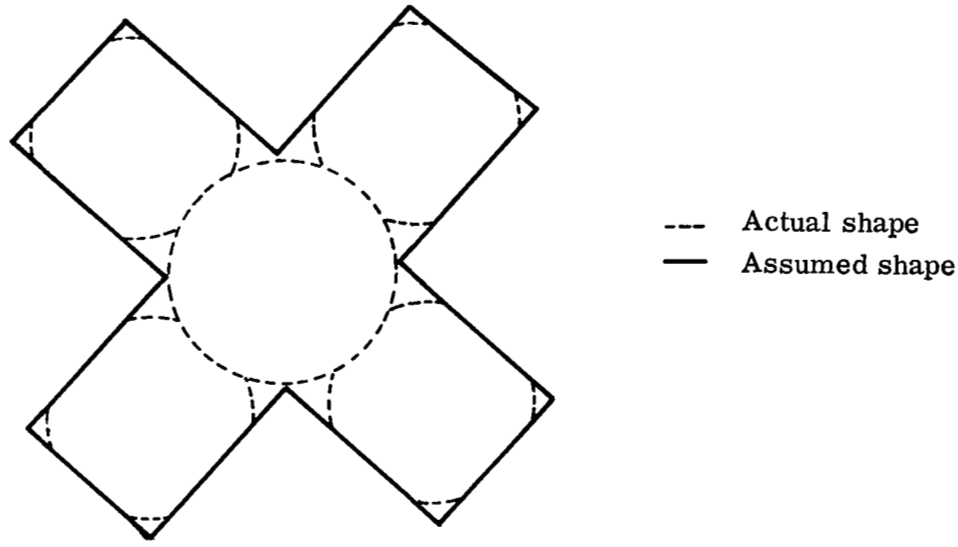

Figure 9.- A cross-sectional model of solar panels used in calculation of effective area of experiments.

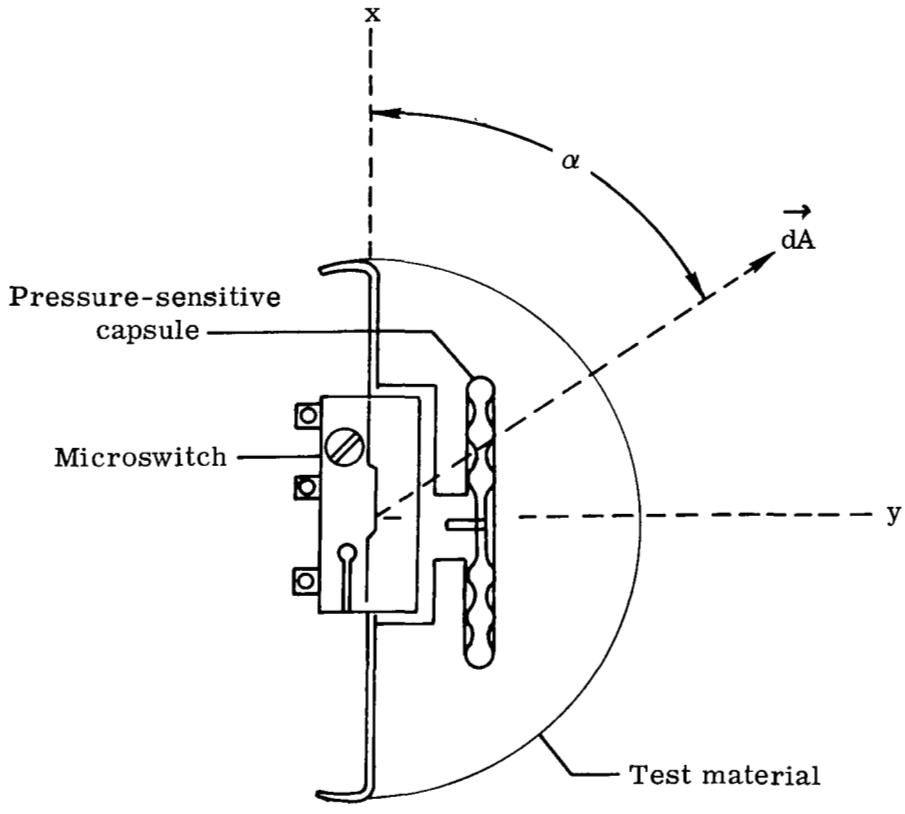

Figure 10.- Cross-sectional view of detector showing coordinate system used in calculation of effective area of experiments.

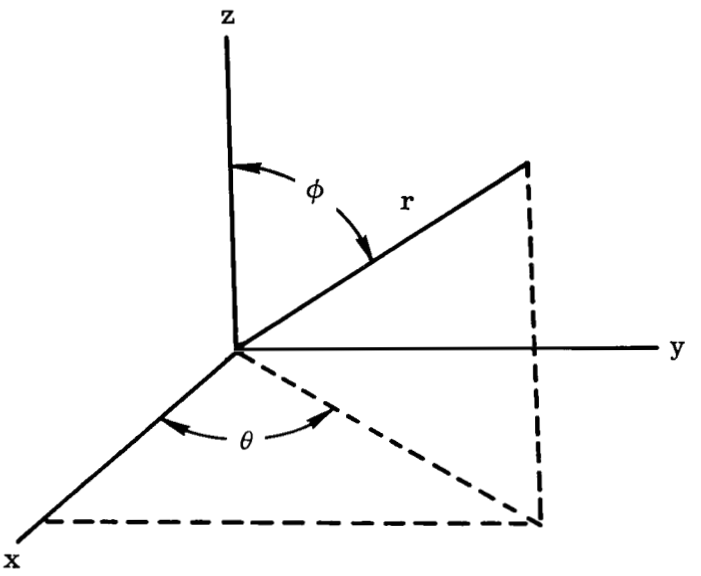

$$x = r \cos \theta \sin \phi$$
$$y = r \sin \theta \sin \phi$$
$$z = r \cos \phi$$

Figure 11.- Spherical coordinate system used in calculations of effective area of experiments. A right-handed system was used for convenience.

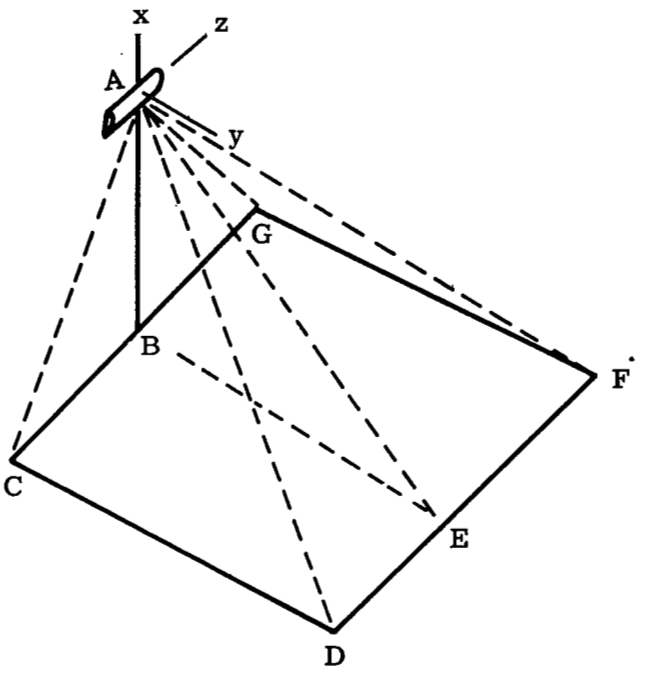

(a) Three-dimensional view.

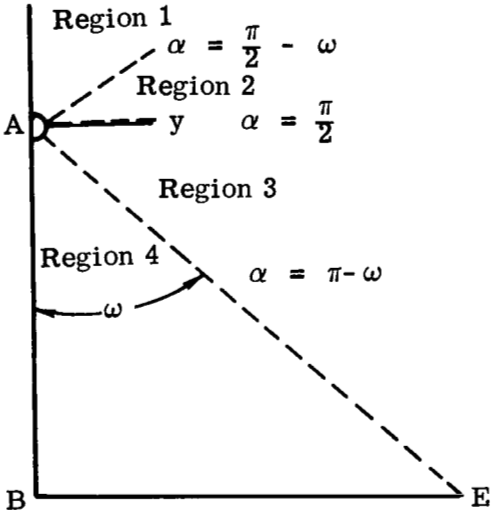

(b) Cross-sectional view.

Figure 12.- Geometry for case I detectors in which dashed lines in (b) separate regions of integration and are designated by different angles of α measured from the +X-axis to the lines.

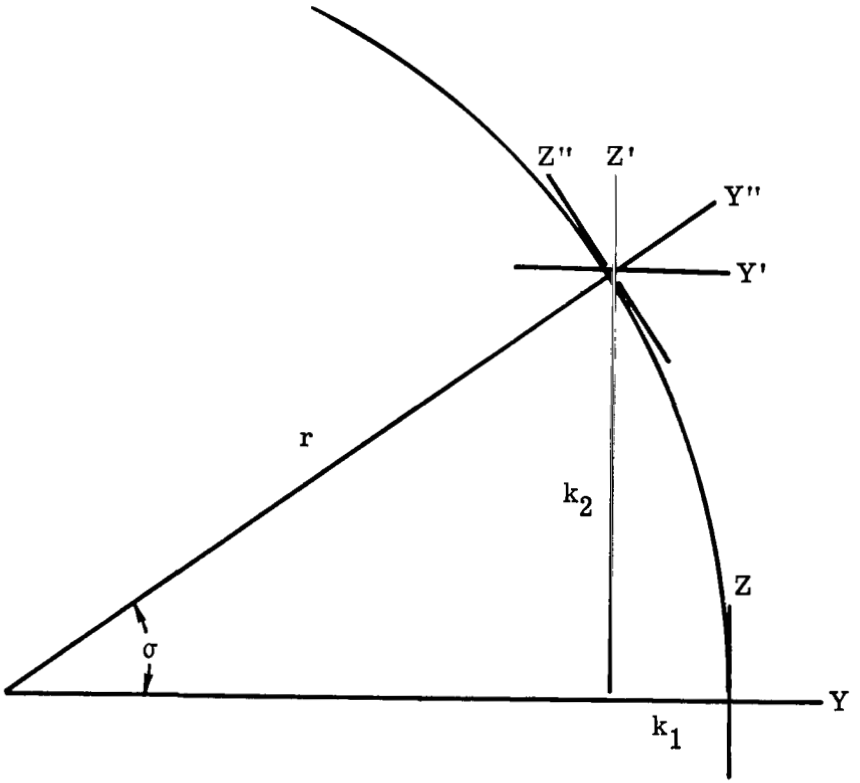

Figure 13.- Geometry for the transformation of equations from X,Y,Z to X'',Y'',Z'' coordinate system in which x'' = x' = x.

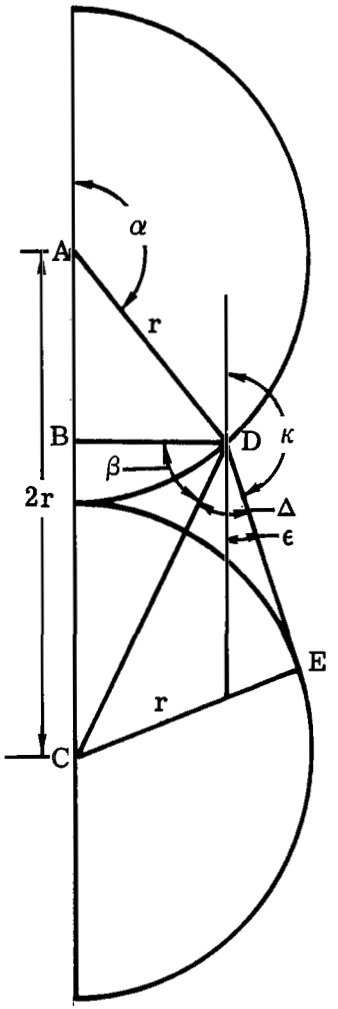

Figure 14.- Geometry for double detector configuration.

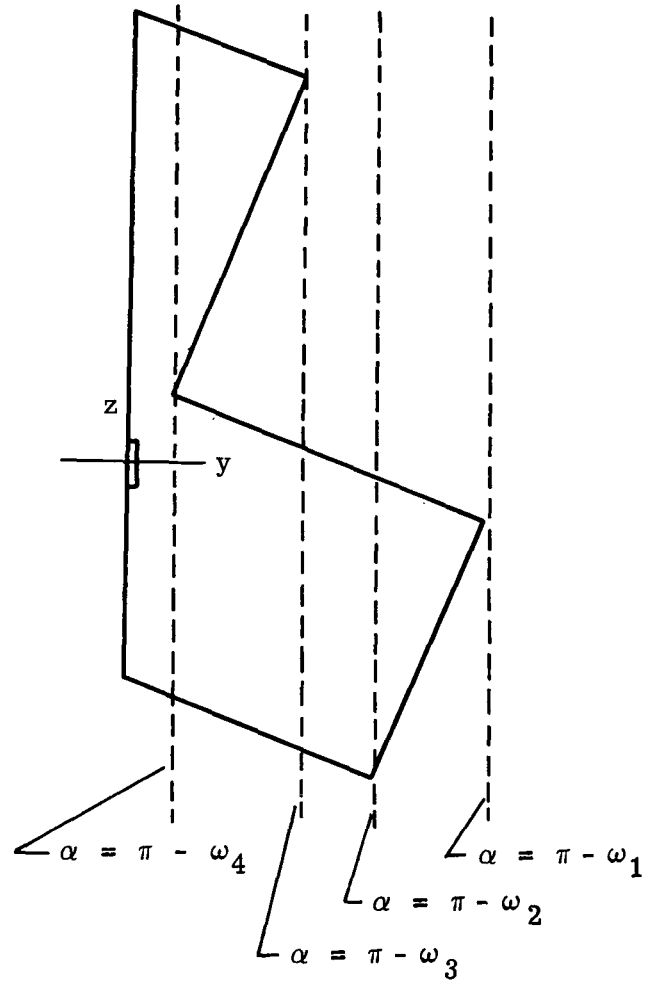

Figure 15.- Geometry for case V detectors with dotted lines showing regions of integration governed by corners of solar panels. The lines are designated by different angles of α measured from the +X-axis to the lines.

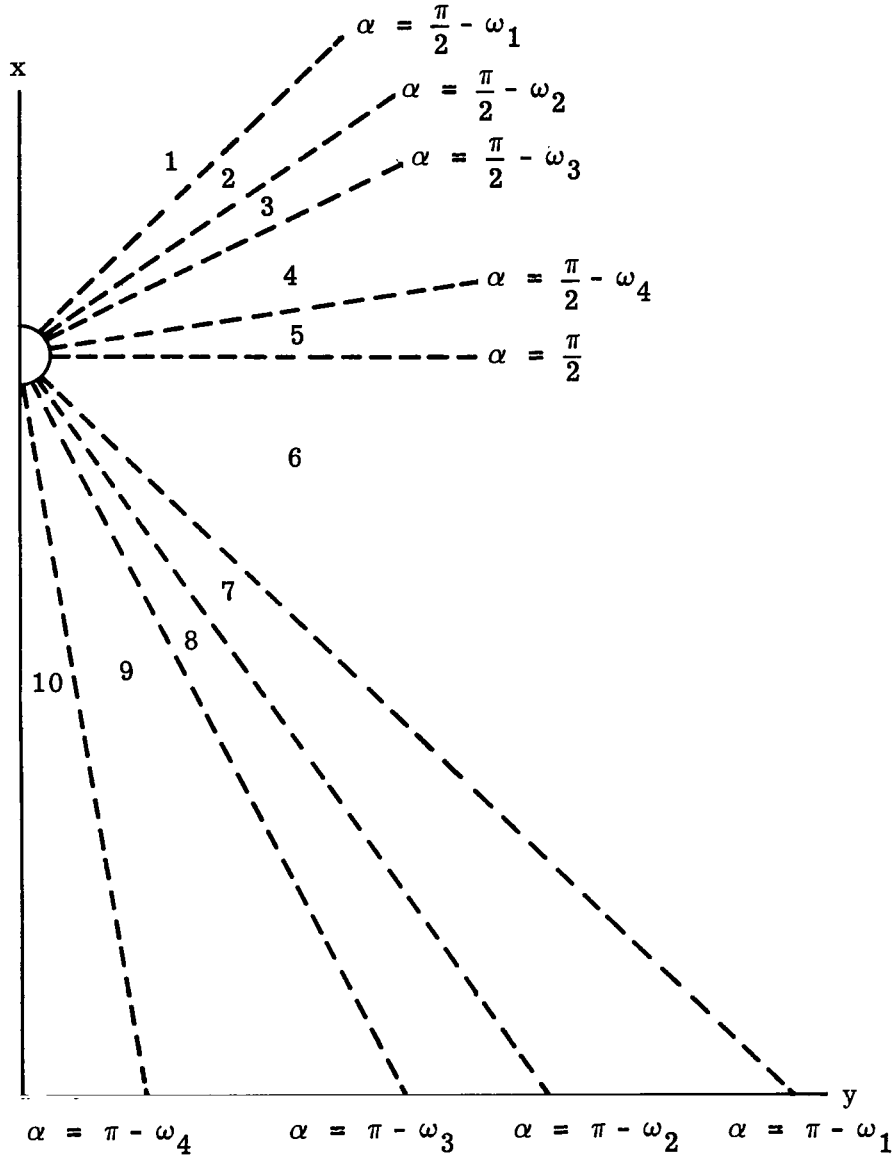

Figure 16.- Geometry for case V detectors in which the dashed lines separate regions of integration and are designated by different angles of α measured from +X-axis to the lines.